CHIN. PHYS. LETT. Vol. 38, No. 11 (2021) 118201

Thermal Management of Air-Cooling Lithium-Ion Battery Pack

Jianglong Du(杜江龙)[1†], Haolan Tao(陶浩兰)[1,2†], Yuxin Chen(陈育新)[1,2†], Xiaodong Yuan(袁小冬)[3], Cheng Lian(练成)[1,2*], and Honglai Liu(刘洪来)[1,2]

[1]*State Key Laboratory of Chemical Engineering, Shanghai Engineering Research Center of Hierarchical Nanomaterials, School of Chemistry and Molecular Engineering, East China University of Science and Technology, Shanghai 200237, China*

[2]*School of Chemical Engineering, East China University of Science and Technology, Shanghai 200237, China*

[3]*Dongtai Middle School, Dongtai 224226, China*

(Received 11 August 2021; accepted 17 September 2021; published online 13 October 2021)

Lithium-ion battery packs are made by many batteries, and the difficulty in heat transfer can cause many safety issues. It is important to evaluate thermal performance of a battery pack in designing process. Here, a multiscale method combining a pseudo-two-dimensional model of individual battery and three-dimensional computational fluid dynamics is employed to describe heat generation and transfer in a battery pack. The effect of battery arrangement on the thermal performance of battery packs is investigated. We discuss the air-cooling effect of the pack with four battery arrangements which include one square arrangement, one stagger arrangement and two trapezoid arrangements. In addition, the air-cooling strategy is studied by observing temperature distribution of the battery pack. It is found that the square arrangement is the structure with the best air-cooling effect, and the cooling effect is best when the cold air inlet is at the top of the battery pack. We hope that this work can provide theoretical guidance for thermal management of lithium-ion battery packs.

DOI: 10.1088/0256-307X/38/11/118201

Rechargeable lithium-ion batteries (LIBs), which are characterized by high capacity, high efficiency, and low self-discharge rate, are widely employed by vehicles, ships, and aircrafts.[1,2] The extensive applications of the LIBs add new requirements for life expectancy, long life and safety.[3–6] The thermal performance of LIBs has great effects on the requirements.[7–9] According to various applications, the batteries are usually manufactured into modules or battery packs through series-parallel connection.[9–11] Therefore, cooling mode and proper module structure play a key role in maintaining uniform and standard temperature level of the batteries.[4,12–14] The following two functions can be realized by using suitable battery temperature management systems to allow the batteries in the pack to work normally:[15–17] (I) The heat of each battery can be effectively dissipated to prevent accidents caused by thermal runaway when the temperature is excessively high. (II) The temperature difference in the pack/module can be reduced, and the whole life of the battery pack can be prevented from falling due to the rapid deterioration of the battery performance. Considering the commercial use, the best heat dissipation system meets not only the above two basic functions but also the requirements of simple structure and low economic cost.

The media such as liquid, phase change material, metal and air play a significant role in battery cooling systems.[5,18,19] As the metal media, micro heat pipe array (MHPA) is commonly used in the lithium-ion battery cooling method due to the characteristics of compactness, and the MHPA can enhance the stability and safety of battery pack.[20] However, the MHPA will reduce the performance of the battery at low temperature.[5] Another effective cooling method is the liquid cooling system because the liquid has good thermal conductivity.[21] However, a liquid cooling system would be limited by high manufacturing cost and space because of its complex structure. Due to the simple structure and low cost, the air-cooling system is more prevailing among these techniques applied in the battery thermal management systems.[22–25] In the battery pack with an air-cooling system, the heat generated from the batteries is dissipated by forced convection of air which is from the ambient or the cooling device.[26,27] The disadvantage of air cooling is uneven heat dissipation and slow cooling speed because of the poor temperature conductivity of air.[28,29] Therefore, in the air-cooling system, appropriate battery pack structure and ventilation structure are significant for battery safety, life and perfor-

Supported by the National Natural Science Foundation of China (Grant Nos. 91834301 and 22078088), the National Natural Science Foundation of China for Innovative Research Groups (Grant No. 51621002), and the Shanghai Rising-Star Program (Grant No. 21QA1401900).

†They contributed equally to this work.

*Corresponding author. Email: liancheng@ecust.edu.cn

© 2021 Chinese Physical Society and IOP Publishing Ltd

mance. Xu and He proved that the heat dissipation performance of the horizontal battery pack were better than that in longitudinal battery pack because of the shorter airflow path.[30] Park demonstrated that the tapered manifold and pressure relief ventilation can improve the cooling performance.[31] Yu designed an air-flow-integrated thermal management system to enhance the temperature uniformity of the lithium ion battery pack.[32] These studies mainly focused on the effects of heat dissipation mode and pack shape on the heat dissipation performance of battery pack. There is a lack of investigation on battery arrangement and cooling-device location in battery pack, which have significant effects on heat dissipation of battery packs.[33]

A lot of equipment and material consumption are required for experiments to study the effect of the battery arrangement and cooling-device location in battery packs,[3] which is uneconomical and inconvenient. Therefore, many battery models have been proposed to study thermal management of lithium ion batteries. In our previous study, an electrode model is proposed to explain the slow charging dynamics of porous electrodes.[34] Compared with the previous model, the pseudo-two-dimensional (P2D) battery model can describe the simultaneous transports in both electrode and electrolyte phase, which make the P2D model applicable under different conditions.[35–37] In this Letter, a P2D battery model and a three-dimensional battery pack model are combined to investigate the thermal performance, and the batteries are arranged together with the forced air-cooling strategies. The main purpose of this study is to evaluate the thermal performance of the battery packs which have different structures by battery arraying in the battery pack with the same number of the battery. Four arrangements of the batteries within the battery pack are employed to investigate the thermal performance, which include square arrangement, rectangular arrangement and two trapezoid arrangements. Moreover, we study the effect of location of the cold air inlet and the effect of size of cold air inlet and outlet in order to optimize the air-cooling system.

Figure 1(a) shows the battery pack which is composed of 25 individual batteries in the air flow compartment. The batteries are cooled with the cold air coming in from the inlet. In the three-dimensional battery pack model, it is assumed that the heat generated by each battery is the same, and the flux and temperature of inlet air at different times remains unchanged. The air flow compartment wall of the battery pack is adiabatic. The air flow in the compartment is described by the Navier–Stokes equation:

$$\rho_{\mathrm{a}}\frac{\partial u_{\mathrm{a}}}{\partial t}+\rho_{\mathrm{a}}u_{\mathrm{a}}\cdot\nabla u_{\mathrm{a}}=-\nabla p+\mu\nabla^2 u_{\mathrm{a}}+F_{\mathrm{e}}, \quad (1)$$

where ρ_{a} is air density, u_{a} is air velocity, μ is air viscosity coefficient, p is pressure, and F_{e} is external force. The boundary condition of the flow chamber wall is $u_{\mathrm{a}}=0$, the boundary condition at the entrance is $u_{\mathrm{a}}=-u_0\hat{n}$, and the boundary condition at the exit is $p=0\,\mathrm{Pa}$.

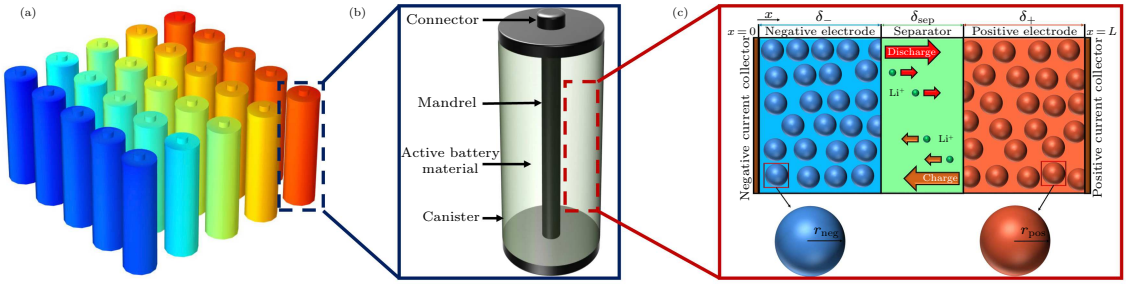

Fig. 1. The battery models: (a) the model of battery pack, (b) the three-dimensional model of individual battery, (c) the pseudo-two-dimensional battery model.

Each battery in the pack is considered as a cylindrical battery as shown in Fig. 1(b). The three-dimensional battery model consists of the following components: cylindrical battery connector on top of the battery (steel), mandrel (nylon isolator around which the battery sheets are wound), active battery material (wound sheets of battery material) and canister. The thickness of the battery canister is not considered since the effect of the steel canister on the temperature profile is small. The components have different physical and chemical properties, so the thermal conductivity of different components is different. In addition, a P2D model is defined to describe the lithium-ion battery, including current collectors, electrodes and separator, as illustrated in Fig. 1(c). The P2D model describes the charge transfer,[38] mass transfer and interfacial reactions (see the Supplementary Material for the governing equation). Here, the P2D model is used to model the chemical properties of the battery, and the three-dimensional model is used to model the temperature distribution of the battery. The two models are coupled by the generated heat source and the average temperature.

The heat source is obtained from the P2D lithium-

ion battery model. During the charging process, the heat is generated because of the intercalation/deintercalation reaction and the ion migration. The generation of heat consists of two parts, one is reversible heat generation due to entropy change, $Q_{\rm rev}$, the other is irreversible heat generation due to joule heating, $Q_{\rm irrev}$.

The molar reversible heat $Q_{{\rm rev},m}$ can be solved by temperature and molar entropy change $\Delta_r S_m$:

$$Q_{{\rm rev},m} = T\Delta_r S_m,$$
$$-\Delta_r S_m = \left[\frac{\partial(\Delta_r G_m)}{\partial T}\right]_p = zF\left(\frac{\partial E}{\partial T}\right)_p, \quad (2)$$

where $\Delta_r G_m$ is the molar reaction Gibbs free energy change. Therefore, the total reversible heat can be expressed as $Q_{\rm rev,total} = -znFT(\partial E/\partial T)_p$, where z is the charge number of ions, n is the mole number of ions participating in the reaction, F is the Faraday constant, T is the temperature, and $(\partial E/\partial T)_p$ is the temperature derivative of equilibrium potential. Irreversible heat is mainly composed of irreversible heat in electrolyte phase and irreversible heat in electrode phase. In porous electrode, irreversible heat can be expressed as $Q_{\rm irrev,por} = JS\eta + JS\Delta\varphi_{\rm e}$, and the irreversible heat in the separator can be expressed as $Q_{\rm irrev,sep} = I\Delta\varphi_{\rm e}$. The total joule heat can be expressed as $Q_{\rm irrev,total} = JS\eta + JS\Delta\varphi_{\rm e} + I\Delta\varphi_{\rm e}$, where η is overpotential, I is the applied current, $\varphi_{\rm e}$ is potential in the liquid phase, S is the area of the electrode plate, and J is the local current density. Therefore, the heat generation in the P2D model can be expressed as $Q_{\rm P2D} = Q_{\rm rev,total} + Q_{\rm irrev,total} = -znFT(\partial E/\partial T)_p + JS\eta + JS\Delta\varphi_{\rm e} + I\Delta\varphi_{\rm e}$.

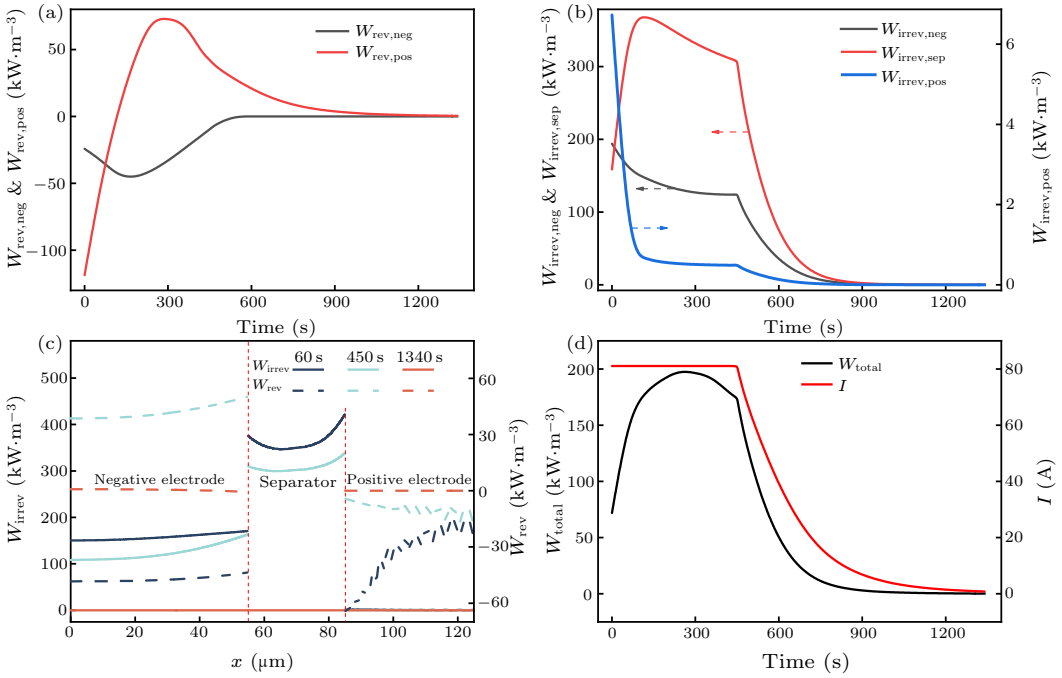

Fig. 2. The heat and current at different positions and times. (a) The time-dependent reversible volume heat density in negative electrode ($W_{\rm rev,neg}$) and positive electrode ($W_{\rm rev,pos}$). (b) The time-dependent irreversible volume heat density in negative electrode ($W_{\rm irrev,neg}$), separator ($W_{\rm irrev,sep}$) and positive electrode ($W_{\rm irrev,pos}$). (c) The location-dependent volume heat density at different times. (d) The time-dependent total volume heat density $W_{\rm total}$ and the current.

Furthermore, we investigate the generation of heat at different positions in the P2D model by introducing the volume power density. The irreversible heat in solid phase, reversible heat in solid phase and irreversible heat in liquid phase can be solved by the following equations, respectively, $W_{\rm irrev,s} = i_v\eta$, $W_{\rm rev,s} = i_v T(\partial E/\partial T)_p$ and $W_{\rm irrev,e} = J\cdot(d\varphi/dx)$, where i_v is volume current density. Figure 2 shows the generation of the heat in the battery charged with constant current and constant voltage, and the constant current is 5 C and the constant voltage is 4.2 V. In addition, the voltage of the battery obtained from the simulation model is compared with the result in the literature (see Fig. S1), in order to demonstrate the reliability of our model.[39] During charging, the reversible heat first appears as heat releases and then with heat absorption, irreversible heat always appears as heat releases as illustrated in Fig. 2(a). The reversible heat in the electrode is positively correlated with $(\partial E/\partial T)_p$, which is a function of the lithium content of electrode phase as shown in Fig. S2. With the progress of charging, the generation of irreversible heat in electrode continuously drops as shown in Fig. 2(b). Because the over potential decreases dur-

ing charging [see Fig. S3(a)], the electric field strength in the separator increases at first and then decreases during charging [see Fig. S3(b)], which leads to the generation of the irreversible heat having a peak. Figure 2(c) shows the location-dependent volume heat density at 60 s (during constant current charge), 450 s (end of constant current charge) and 1340 s (end of constant voltage charge) of charging. Irreversible heat is generated at the separator more than that at the electrode. At the beginning of charging, the positive electrode generates more reversible heat on the side close to the separator and more on the side far from the separator at the later stage. The change trend of total battery heat with time is the same as that of irreversible heat as shown in Fig. 2(d). During constant current charging, the total heat generation of the battery reaches its maximum value. During constant voltage charging, the heat generation of the battery decreases with the decrease of current.

To couple the P2D battery model with the three-dimensional thermal model, the heat generated from the P2D battery model is distributed to the three-dimensional battery model, $Q_{3D} = Q_{\mathrm{P2D}}$. In the three-dimensional battery model, the heat balance can be described by the equation $\rho C_p(\partial T/\partial t) + \rho C_p u \cdot \nabla T + \nabla q = Q$, $q = -k\nabla T$, where ρ is the density of the active material, C_p is the specific heat capacity of the active material, u is the heat convection velocity, and k is the thermal conductivity of the material. The bottom and top of the battery are insulated, $-\hat{n}q = 0$.

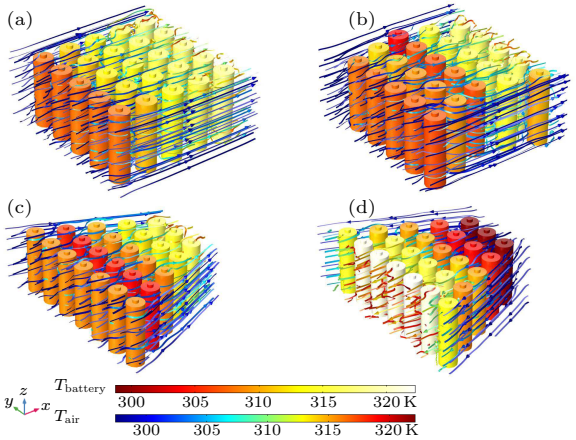

Fig. 3. Temperature distribution of the battery packs with different battery arrangements at the end of 5 C charging rate: (a) square arrangement, (b) stagger arrangement, (c) trapezoid arrangement (left surface is the air inlet), (d) trapezoid arrangement (right surface is the air inlet).

Figure 3 shows the four battery arrangements investigated, including square arrangement (case I), stagger arrangement (case Ⅱ), trapezoidal arrangement whose air inlet is on the left surface (case Ⅲ) and trapezoidal arrangement whose air inlet is on the right surface (case Ⅳ). The temperature measurement results for each pack with different battery arrangements at the end of charging are shown, and the ribbon with the arrow represents the flowing air. In all four cases the air temperature at the inlet is 25° and the air flux is 1.458 m^3/s.

Compared with the temperature of the pack without air cooling shown in Fig. S2, the temperature of the battery packs with the cooling system is obviously reduced. As shown in Fig. 3, the temperature distributions at the inlet and outlet are different. The battery temperature at the inlet is lower than that at the outlet due to the heat exchange between the air and batteries. For case I [Fig. 3(a)], the battery temperature in the square pack increases along the direction of air flow, and the temperature of the battery at the same distance from the inlet is similar. For the pack with battery stagger arrangement (case Ⅱ), the battery temperatures are different at the same x position as shown in Fig. 3(b). The stagger arrangement makes some batteries close to the wall. Therefore, the batteries near the wall are exposed to less heat source (other batteries) and have lower temperature. This reduces the temperature of some batteries, but increases the non-uniformity of the temperature distribution within the battery pack. Figures 3(c) and 3(d) show the temperature distribution in the pack with battery trapezoid arrangements. The cold air inlet is at the left surface of the trapezoid in case Ⅲ and at the right in case Ⅳ, respectively. In order to keep the cold air flux consistent with other cases, the cold air flow rate at the inlet of case Ⅳ is the fastest because of the small inlet area. Therefore, the battery temperature near the cold air inlet is lowest in case Ⅳ.

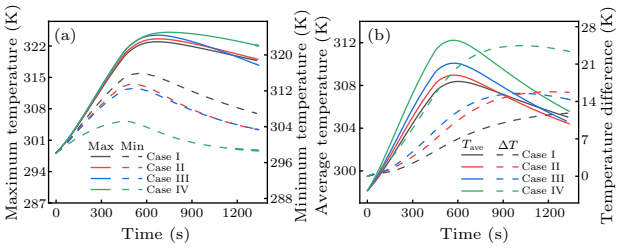

Fig. 4. The time-dependent temperature in different battery packs during charging: (a) the maximum temperature (solid line) and minimum temperature (dotted line) in the battery packs, (b) the average temperature (solid line) and the maximum temperature difference between different positions in the battery pack (dotted line).

Figure 4 shows the time-dependent temperature in different battery packs. The battery pack in case Ⅳ has the lowest minimum temperature and the highest maximum temperature, which is consistent with the result shown in Fig. 3(d). Among the four cases, the maximum value of the battery temperature in case I is the smallest, and the minimum value in case I is the largest. This reduces the temperature difference

between different positions of the battery pack in case I as shown in Fig. 4(b). It is found that the average battery pack temperature is from low to high as follows: case I, case Ⅱ, case Ⅲ, and case Ⅳ. In addition, the maximum temperature difference between different positions in the battery pack is from small to large as follows: case I, case Ⅱ, case Ⅲ, and case Ⅳ. Therefore, the best battery arrangement for the heat dissipation performance of battery packs is the square arrangement. This result is consistent with the result in the literature.[4] For square arrangement, the flowing air in the battery pack has a lower temperature because it has a short flow path, which results in a higher convection conductivity in case I than those in other cases. The higher convection conductivity enhances the heat exchange efficiency between the batteries and the cold air. The square arrangement has a simple structure and can be used in commercial batteries to reduce economic costs. Due to its excellent heat dissipation, square arrangements can be applied in many aspects.

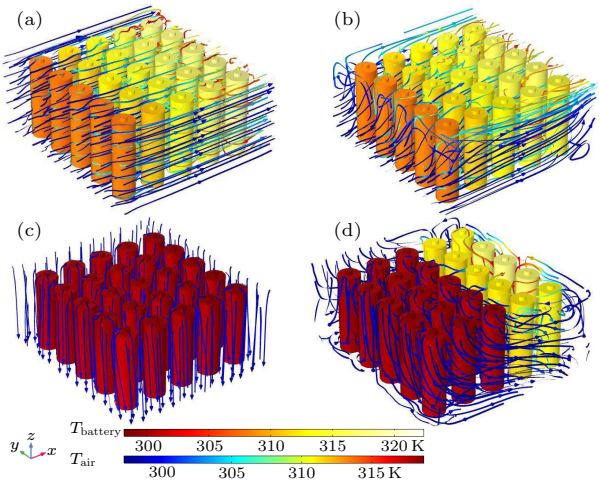

Fig. 5. Temperature distribution of the battery packs with different inlet and outlet positions at the end of 5 C charging rate.

The purpose of forced air cooling is to reduce the battery temperature. The direction and path of the air flow have a great influence on the cooling effect and the uniformity of temperature.[33] Previous studies focused on the interior structure of the battery pack rather than the location of the cooling device.[40,41] Here, the battery thermal performance is studied when the air inlet and outlet are located at different positions of the battery pack as shown in Fig. 5. There are 4 situations considered: (a) inlet at the left surface and outlet at the right (case I), (b) inlet at the lower half of the left surface and outlet at the upper half of the right surface (case V), (c) inlet at the top and outlet at the bottom (case Ⅵ), (d) inlet at the left half of the top surface and outlet at the right half of the bottom surface (case Ⅶ). The cold air fluxes of the four strategies are consistent with each other.

Figure 5 shows the temperature distribution in the battery pack with different inlet and outlet positions. The effect of the forced air cooling with different device locations is distinguished by observing the temperature of the battery surface. The battery temperature distribution pattern of the battery pack with different air inlet positions has the same phenomenon: the temperature near the air outlet side and in the middle of the battery module is higher, while the temperature near the inlet is closest to the ambient temperature. In case Ⅶ, the temperature difference between the battery at the inlet and outlet is close to 20 K. The most effective cooling strategy is that the cold air inlet is located on the top of the battery pack, as shown in Fig. 5(c). In case Ⅵ, all batteries have low temperatures and uniform temperature distribution.

Figure 6 shows the time-dependent temperature of battery packs with different inlet and outlet locations. The battery packs in cases I, V and Ⅶ have similar maximum temperatures, while the pack in case Ⅵ has the lowest maximum temperature, as shown in Fig. 6(a). In addition, the battery pack in case Ⅵ has the lowest average temperature as shown in Fig. 6(b), and the battery pack in case Ⅵ has the smallest temperature difference at the end of charging. It indicates that the most effective cooling strategy is case Ⅵ, which is consistent with the above result.

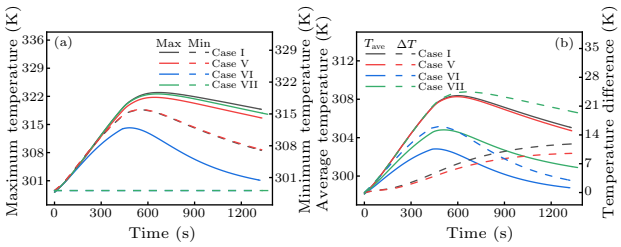

Fig. 6. The time-dependent temperature in battery packs with different inlet and outlet positions during charging: (a) the maximum temperature (solid line) and minimum temperature (dotted line) in the battery packs, (b) the average temperature (solid line) and the maximum temperature difference between different positions in the battery pack (dotted line).

In summary, we have investigated the effect of battery arrangement and location of an air-cooling device on thermal performance of the battery pack. Four arrangements are employed to explore the thermal performance: one square arrangement, one stagger arrangement and two trapezoid arrangements. The results show that the cooling effect of the battery pack with the square arrangement is optimal. On this basis, we have also studied the cooling effect of the inlet and outlet position on the battery pack. The temperature distribution of batteries is described based on different cooling device locations, and the conclusion is arrived as follows: the best cooling performance is

arrived when the cool air inlet is on the top of the pack and the entire upper surface is the inlet. The cooling effect of forced cold air depends on its speed, temperature and flow path. The short flow path allows cold air to take more heat away per unit time. When the air-cooling device is on the top and the air outlet on the bottom, the air flow path is short. That is why the cooling effect in case VI is the best among all the cases, which can guide design of safe and efficient battery packs.

References

[1] Xiong R, Sun F, Gong X and Gao C 2014 *Appl. Energy* **113** 1421
[2] Xiong R, Sun F, Chen Z and He H 2014 *Appl. Energy* **113** 463
[3] Rad M S, Danilov D L, Baghalha M, Kazemeini M and Notten P H L 2013 *Electrochim. Acta* **102** 183
[4] Kang D, Lee P Y, Yoo K and Kim J 2020 *Journal of Energy Storage* **27** 101017
[5] Wang L, Zhao Y, Quan Z and Liang J 2021 *J. Energy Storage* **39** 102624
[6] Qiao R X, Zhang M J, Liu Y D, Ren W J, Lin Y and Pan F 2016 *Chin. Phys. Lett.* **33** 078201
[7] Ng S S Y, Xing Y and Tsui K L 2014 *Appl. Energy* **118** 114
[8] Ping P, Wang Q, Huang P, Sun J and Chen C 2014 *Appl. Energy* **129** 261
[9] Siruvuri S V and Budarapu P 2020 *J. Energy Storage* **29** 101377
[10] Pan Y, Feng X, Zhang M, Han X, Lu L and Ouyang M 2020 *J. Cleaner Production* **255** 120277
[11] Li X, Xu J, Hong J, Tian J and Tian Y 2021 *Energy* **214** 118858
[12] Wang T, Tseng K J, Zhao J and Wei Z 2014 *Appl. Energy* **134** 229
[13] Huang Q, Li X, Zhang G, Deng J and Wang C 2021 *Appl. Thermal Engin.* **183** 116151
[14] Luo X, Guo Q, Li X, Tao Z, Lei S, Liu J, Kang L, Zheng D and Liu Z 2020 *Renew. Energy* **145** 2046
[15] Qian Z, Li Y and Rao Z 2016 *Energy Conversion and Management* **126** 622
[16] Greco A, Cao D, Jiang X and Yang H 2014 *J. Power Sources* **257** 344
[17] Zhao R, Zhang S, Liu J and Gu J 2015 *J. Power Sources* **299** 557
[18] Lu M, Zhang X, Ji J, Xu X and Zhang Y 2020 *J. Energy Storage* **27** 101155
[19] Zhao G, Wang X, Negnevitsky M and Zhang H 2021 *J. Power Sources* **501** 230001
[20] Ye X, Zhao Y and Quan Z 2018 *Appl. Thermal Engin.* **130** 74
[21] Shang Z, Qi H, Liu X, Ouyang C and Wang Y 2019 *Int. J. Heat Mass Transfer* **130** 33
[22] Xie J, Ge Z, Zang M and Wang S 2017 *Appl. Thermal Engin.* **126** 583
[23] Yang T, Yang N, Zhang X and Li G 2016 *Int. J. Thermal Sci.* **108** 132
[24] Saw L H, Ye Y, Tay A A, Chong W T, Kuan S H and Yew M C 2016 *Appl. Energy* **177** 783
[25] Wang T, Tseng K and Zhao J 2015 *Appl. Thermal Engin.* **90** 521
[26] Yang W, Zhou F, Zhou H and Liu Y 2020 *Int. J. Heat Mass Transfer* **161** 120307
[27] Behi H, Karimi D, Behi M, Ghanbarpour M, Jaguemont J, Sokkeh M A, Gandoman F H, Berecibar M and Van Mierlo J 2020 *Appl. Thermal Engin.* **174** 115280
[28] Chen D, Jiang J, Kim G H, Yang C and Pesaran A 2016 *Appl. Thermal Engin.* **94** 846
[29] Kizilel R, Sabbah R, Selman J R and Al-Hallaj S 2009 *J. Power Sources* **194** 1105
[30] Xu X and He R 2013 *J. Power Sources* **240** 33
[31] Park H 2013 *J. Power Sources* **239** 30
[32] Deng C, Yao Z, Yu X, Yuan C, Li Z and Su L 2014 *IEEE Conference and Expo Transportation Electrification Asia-Pacific (ITEC Asia-Pacific)*, 31 August–3 September 2014, Beijing, pp 1–4
[33] Liu H, Wei Z, He W and Zhao J 2017 *Energy Conversion and Management* **150** 304
[34] Lian C, Janssen M, Liu H and van Roij R 2020 *Phys. Rev. Lett.* **124** 076001
[35] Doyle M, Fuller T F and Newman J 1993 *J. Electrochem. Soc.* **140** 1526
[36] Aurbach D, Ein-Ely Y and Zaban A 1994 *J. Electrochem. Soc.* **141** L1
[37] Levi M D and Aurbach D 1997 *J. Electroanal. Chem.* **421** 79
[38] Du J, Tao H, Yang J, Lian C, Lin S and Liu H 2021 *Chin. J. Chem. Engin.* **31** 33
[39] Yudha C S, Muzayanha S U, Widiyandari H, Iskandar F, Sutopo W and Purwanto A 2019 *Energies* **12** 1886
[40] Chung Y and Kim M S 2019 *Energy Conversion and Management* **196** 105
[41] Pesaran A A 2001 *Battery Man* **43**(5) 34

Supplementary Material for "Thermal Management of Air-Cooling Lithium-Ion Battery Pack"

Conversation equations

The partial differential equations (PDEs) are employed to describe the conservation of charge and mass in solid and liquid phases. In the pseudo-two-dimensional model, the active electrode material is considered to be composed of uniform spherical particles with the same size.

Fick's second law is used to describe the diffusion of lithium ions in particles.

$$\frac{\partial c_{s,i}}{\partial t} = \frac{D_{s,i}}{r^2}\frac{\partial}{\partial r}\left(r^2 \frac{\partial c_{s,i}}{\partial r}\right) \tag{1}$$

where $i = n \,\&\, p$, n is the negative electrode, p is the positive electrode, $c_{s,i}$ is the lithium-ion concentration in the solid phases, $D_{s,i}$ is the lithium-ion diffusion coefficient in the solid phases. The boundary conditions are as follows,

$$\left.\frac{\partial c_{s,i}}{\partial r}\right|_{r=0} = 0, D_{s,i}\left.\frac{\partial c_{s,i}}{\partial r}\right|_{r=R_{s,i}} = -\frac{J_i}{a_{v,i}F} \tag{2}$$

where $R_{s,i}$ is the radius of spherical material particles, J_i is the local current density, and $a_{v,i}$ is the specific surface area of spherical material particles.

Based on the concentrated solution theory, the concentration of lithium ion in the liquid phase of porous electrode can be described by the following equation,

$$\varepsilon_{e,i}\frac{\partial c_e}{\partial t} = \frac{\partial}{\partial x}\left(D_{e,i}^{eff}\frac{\partial c_e}{\partial x}\right) + a_{v,i}t_0^+\frac{J_i}{F} \tag{3}$$

where $\varepsilon_{e,i}$ is the volume fraction of liquid phase, $D_{e,i}^{eff}$ is the effective diffusion coefficient of lithium ion in liquid phase, and t_0^+ is the lithium ion migration number. The boundary condition is,

$$\begin{cases} \left.D_{e,i}^{eff}\frac{\partial c_e}{\partial x}\right|_{x=0} = 0, \left.D_{e,i}^{eff}\frac{\partial c_e}{\partial x}\right|_{x=L} = 0 \\ \left.D_{e,i}^{eff}\frac{\partial c_e}{\partial x}\right|_{x=(\delta_-)^-} = \left.D_{e,i}^{eff}\frac{\partial c_e}{\partial x}\right|_{x=(\delta_-)^+}, \left.D_{e,i}^{eff}\frac{\partial c_e}{\partial x}\right|_{x=(\delta_- + \delta_{sep})^-} = \left.D_{e,i}^{eff}\frac{\partial c_e}{\partial x}\right|_{x=(\delta_- + \delta_{sep})^+} \\ \left.c_e\right|_{x=(\delta_-)^-} = \left.c_e\right|_{x=(\delta_-)^+}, \left.c_e\right|_{x=(\delta_- + \delta_{sep})^-} = \left.c_e\right|_{x=(\delta_- + \delta_{sep})^+} \end{cases} \tag{4}$$

The charge conservation in porous electrode is described by Ohm's law,

$$\sigma_i^{eff}\frac{\partial \varphi_{s,i}}{\partial x} = J_i \tag{5}$$

where σ_i^{eff} is the effective conductivity in the solid phase and $\varphi_{s,i}$ is the potential

in solid phase. Here we consider that the negative electrode is electrically grounded, and the boundary condition is,

$$\varphi_s\big|_{x=0} = 0\ \mathrm{V}, -\sigma_n^{eff}\left.\frac{\partial \varphi_s}{\partial x}\right|_{x=\delta_-} = -\sigma_i^{eff}\left.\frac{\partial \varphi_s}{\partial x}\right|_{x=\delta_-+\delta_{sep}} = 0, -\sigma_i^{eff}\left.\frac{\partial \varphi_s}{\partial x}\right|_{x=\delta_-+\delta_{sep}+\delta_+} = \frac{I_{app}}{A} \quad (6)$$

where I_{app} is the applied current.

The charge conservation in the liquid phase of the porous electrode is described by the following equation,

$$\kappa_i^{eff}\frac{\partial \varphi_e}{\partial x} = -J_i + \kappa_i^{eff}\frac{2RT}{F}\left(1-t_0^+\right)\left[1+\frac{\partial \ln f}{\partial \ln\left(\frac{c_e}{c^\Theta}\right)}\right]\frac{\partial \ln\left(\frac{c_e}{c^\Theta}\right)}{\partial x} \quad (7)$$

where κ_i^{eff} is the lithium-ion effective conductivity in liquid phase, f is the activity coefficient, c^Θ is the standard concentration, $c^\Theta = 1\ \mathrm{mol\cdot m^{-3}}$. The boundary condition is,

$$\begin{cases} \left.\frac{\partial \varphi_{e,i}}{\partial x}\right|_{x=0} = \left.\frac{\partial \varphi_{e,i}}{\partial x}\right|_{x=\delta_-+\delta_{sep}+\delta_+} = 0 \\ -\kappa_i^{eff}\left.\frac{\partial \varphi_e}{\partial x}\right|_{x=(\delta_-)^+} = -\kappa_i^{eff}\left.\frac{\partial \varphi_e}{\partial x}\right|_{x=(\delta_-)^-}, -\kappa_i^{eff}\left.\frac{\partial \varphi_e}{\partial x}\right|_{x=(\delta_-+\delta_{sep})^+} = -\kappa_i^{eff}\left.\frac{\partial \varphi_e}{\partial x}\right|_{x=(\delta_-+\delta_{sep})^-} \end{cases} \quad (8)$$

The liquid concentration in the separator is described by the following equation,

$$\varepsilon_{e,sep}\frac{\partial c_e}{\partial t} = \frac{\partial}{\partial x}\left(D_{e,sep}^{eff}\frac{\partial c_e}{\partial x}\right) \quad (9)$$

where $\varepsilon_{e,sep}$ is the volume fraction of liquid phase, and $D_{e,sep}^{eff}$ is the effective diffusion coefficient of lithium ion in the liquid phase in the separator. The boundary condition is,

$$\left.\frac{\partial c_e}{\partial x}\right|_{x=\delta_+} = \left.\frac{\partial c_e}{\partial x}\right|_{x=\delta_++\delta_{sep}} = 0 \quad (10)$$

The potential in the separator is described by the following equation,

$$\kappa_{sep}^{eff}\frac{\partial \varphi_e}{\partial x} = -\frac{I_{app}}{A} + \kappa_{sep}^{eff}\frac{2RT}{F}\left(1-t_0^+\right)\left[1+\frac{\partial \ln f}{\partial \ln\left(\frac{c_e}{c^\Theta}\right)}\right]\frac{\partial \ln\left(\frac{c_e}{c^\Theta}\right)}{\partial x} \quad (11)$$

where A is the area of the electrode plate and κ_{sep}^{eff} is the effective conductivity of the liquid phase in the separator. The boundary conditions are as follows,

$$\left.\frac{\partial \varphi_e}{\partial x}\right|_{x=\delta_+} = \left.\frac{\partial \varphi_e}{\partial x}\right|_{x=\delta_+ +\delta_{sep}} = 0 \tag{12}$$

In addition, there are some additional equations to describe some of the above physical quantities,

$$\begin{cases} a_{v,i} = \dfrac{3\varepsilon_{s,i}}{R_{s,i}}, i = n, p \\ D_{e,i}^{eff} = D_{e,i}\varepsilon_{e,i}^{1.5}, i = n, sep, p \\ \sigma_i^{eff} = \sigma_i \varepsilon_{s,i}^{1.5}, i = n, p \\ \kappa_i^{eff} = \kappa_i \varepsilon_{e,i}^{1.5}, i = n, sep, p \end{cases} \tag{13}$$

where $D_{e,i}$ is the lithium-ion diffusion coefficient in liquid phase, σ_i is the solid conductivity and κ_i is the liquid conductivity.

Butler-Volmer equation are used to describe the relationship between the local current density at the solid-liquid interface and the overpotential of intercalation/deintercalation reaction,

$$J = i_0 \left[\exp\left(\frac{\alpha_a F}{RT} \eta \right) - \exp\left(\frac{-\alpha_c F}{RT} \eta \right) \right] \tag{14}$$

where i_0 is the exchange current density, which is determined by the concentration of lithium ion in the liquid phase and the concentration of lithium ion at the solid-liquid interface, $i_0 = k_a \left(\mathrm{c}_{s,\max} - \mathrm{c}_{s,surf} \right)^{\alpha_c} c_{s,surf}^{\alpha_a} c_e^{\alpha_a}$, where k_a is the rate constant of intercalation/deintercalation reaction, α_a and α_c is the anode transfer coefficient and the cathode transfer coefficient, respectively. η is the overpotential which is related to solid phase potential, liquid phase potential and equilibrium potential, $\eta = \varphi_s - \varphi_e - E_{eq}$.

Physical properties

Table 1 presents the geometric parameters required for pseudo-two-dimensional model and the physical quantities required for numerical simulation. Table 2 presents the geometric parameters required for single battery model and the battery pack model.

Table 1. Parameter of the pseudo-two-dimensional model

Parameter	Value	Parameter	Value
Length of negative electrode (δ_{neg})	5.5×10^{-5} m	Charging cutoff voltage ($E_{\max}$)	4.1 V
Length of separator (δ_{sep})	3×10^{-5} m	Discharging cutoff voltage ($E_{\min}$)	2.5 V
Length of positive electrode (δ_{pos})	4×10^{-5} m	Initial lithium ion concentration in electrolyte ($c_{e,0}$)	1200 mol/m^3
Particle radius of positive electrode material (r_{pos})	2.5×10^{-7} m	Volume fraction of material in positive electrode ($\varepsilon_{s,pos}$)	0.42
Initial lithium-ion concentration in positive electrode ($c_{pos,\max}$)	48000 mol/m^3	Volume fraction of other filling in positive electrode ($\varepsilon_{f,pos}$)	0.17
Concentration of chloride ion in the electrolyte ($c_{cl,e}$)	1200 mol/m^3	Volume fraction of electrolyte in positive electrode ($\varepsilon_{e,pos}$)	0.41
Exchange current density in positive electrode ($I_{0,pos}$)	36.61 A/m^2	Exchange current density in negative electrode ($I_{0,neg}$)	0.96 A/m^2

Table 2. Parameter of the battery pack model

Parameter	Value	Parameter	Value
Battery radius (r_{batt})	9 mm	Inlet temperature (T_{inlet})	298.15 K
Battery height (h_{batt})	65 mm	Initial temperature (T_{init})	298.15 K
Mandrel radius ($r_{mandrel}$)	2 mm	Connector radius ($r_{connector}$)	0.003 m
Battery thermal conductivity, angular ($k_{T,batt,ang}$)	32.512 W/(m ·K)	Connector height ($h_{connector}$)	0.003 m
Battery thermal conductivity, radial ($k_{T,batt,r}$)	0.85807 W/(m ·K)	Air velocity at the entrance	3.159×10^{-6} m^3/s
Battery density (ρ_{batt})	2026.4 kg/m ^{3}	Battery heat capacity ($C_{p,batt}$)	1412.8 J/(kg ·K)

Numerical model validation

The voltage of the battery obtained from the simulation model is compared with the result in the literature, in order to demonstrate the reliability of our model[1]. The voltage rise rate gradually decreases as charging as shown in Fig. S1. The maximum error of the voltage between the experiment and simulation results does not exceed 0.2 V. It proves that our mathematical model is reasonable.

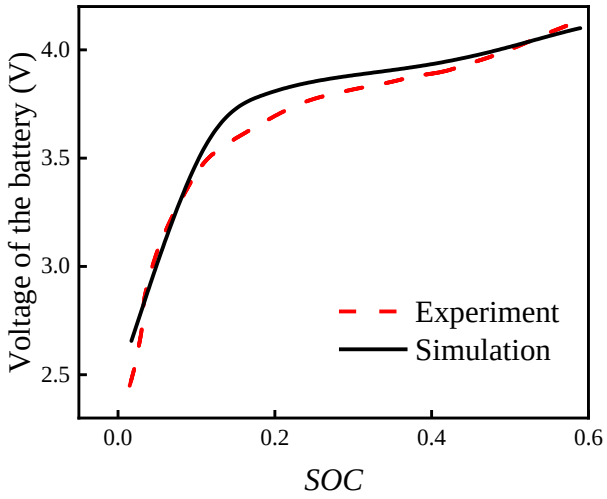

Figure S1. The voltage of the battery obtained by experiment and simulation

Thermal analysis of battery pack without forced air cooling

Fig. S2 shows the temperature distribution in the battery pack at the end of a single charge-discharge cycle without air cooling. The result shows that the temperature in the pack is high and the temperature distribution is uniform. During the charging process, each battery is considered as a heat source. In addition to the heat generated by the battery itself, the heat generated by the surrounding batteries will also cause the temperature of the battery to rise. The highest temperature of the pack is 325 K, which is not the proper operating temperature. Therefore, the forced air-cooling system is applied into the battery pack for the operational stability and safety.

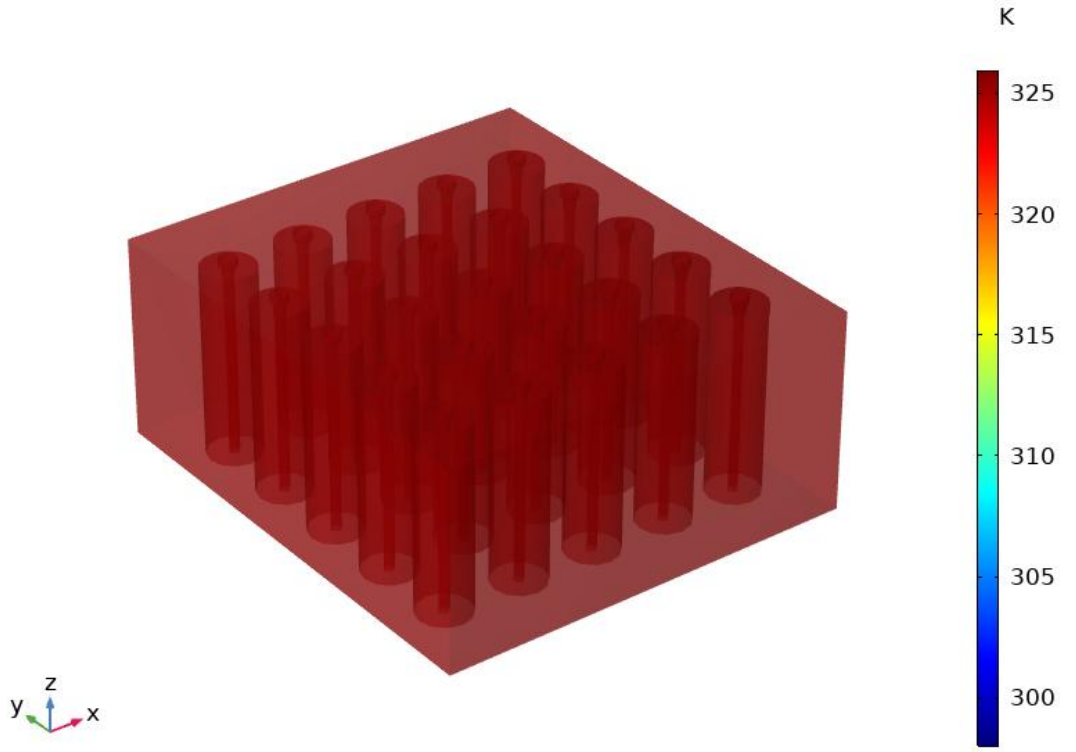

Figure S2. The temperature distribution of the battery pack without air-cooling system

Fig. S3 and Fig. S4 show the time-dependent temperature in different battery pack using stagger arrangement and trapezoid arrangement. For the staggered arrangement and trapezoidal arrangement, the ventilation strategy with air inlet above and outlet below is the best. As shown in Fig. S3 and Fig. S4, the batteries in the battery packs have low temperatures and uniform temperature distribution when the air-cooling device is on the top and the air outlet on the bottom.

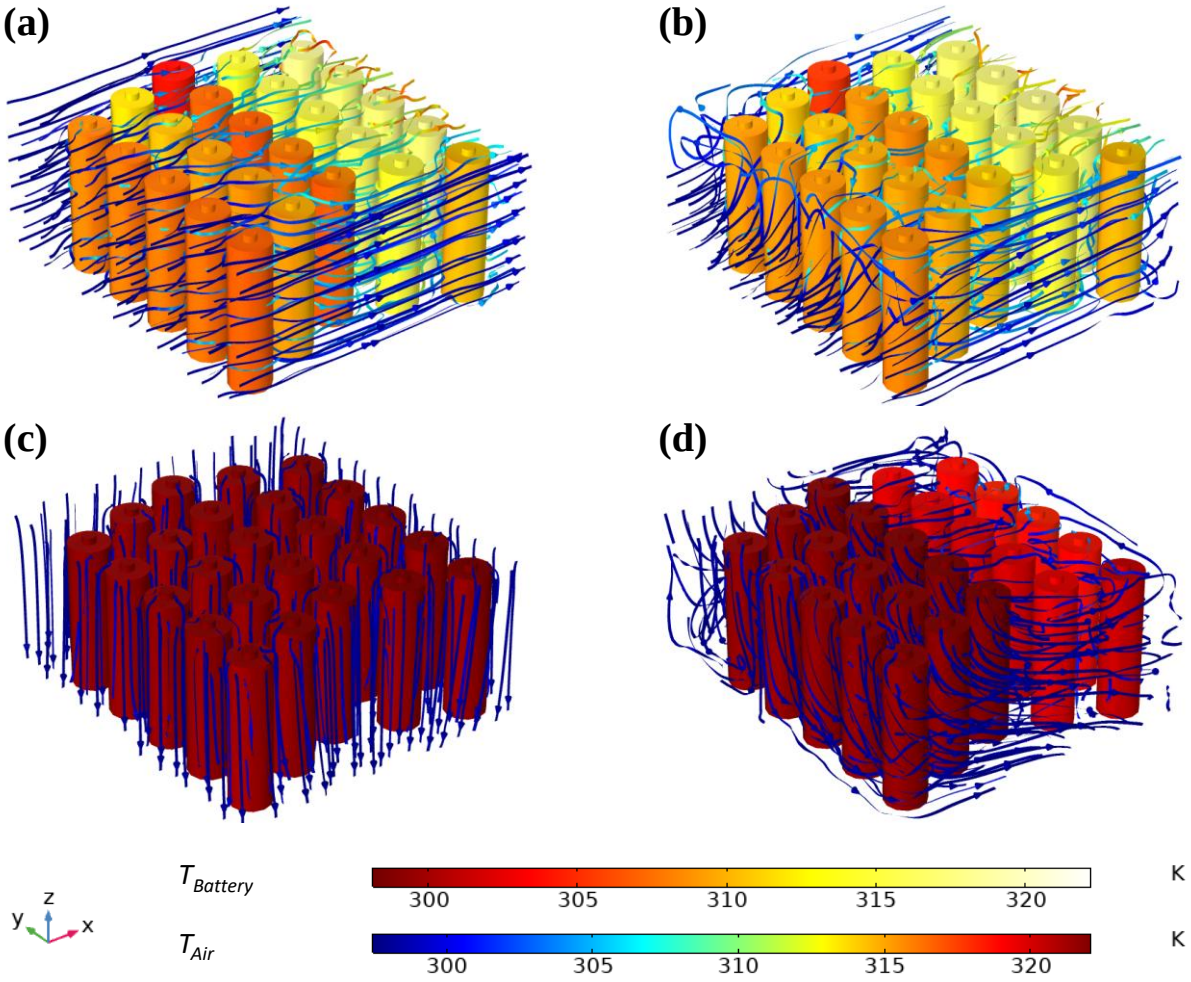

Figure S3. Temperature distribution of the battery packs with different inlet and outlet positions for stagger arrangement. (a) The air inlet is on the left and the outlet is on the right. (b) The air inlet is on the lower left side and the outlet is on the upper right side. (c) The air inlet is on the upper side and the outlet is on the lower side. (d) The air inlet is on the upper left and the outlet is on the lower right.

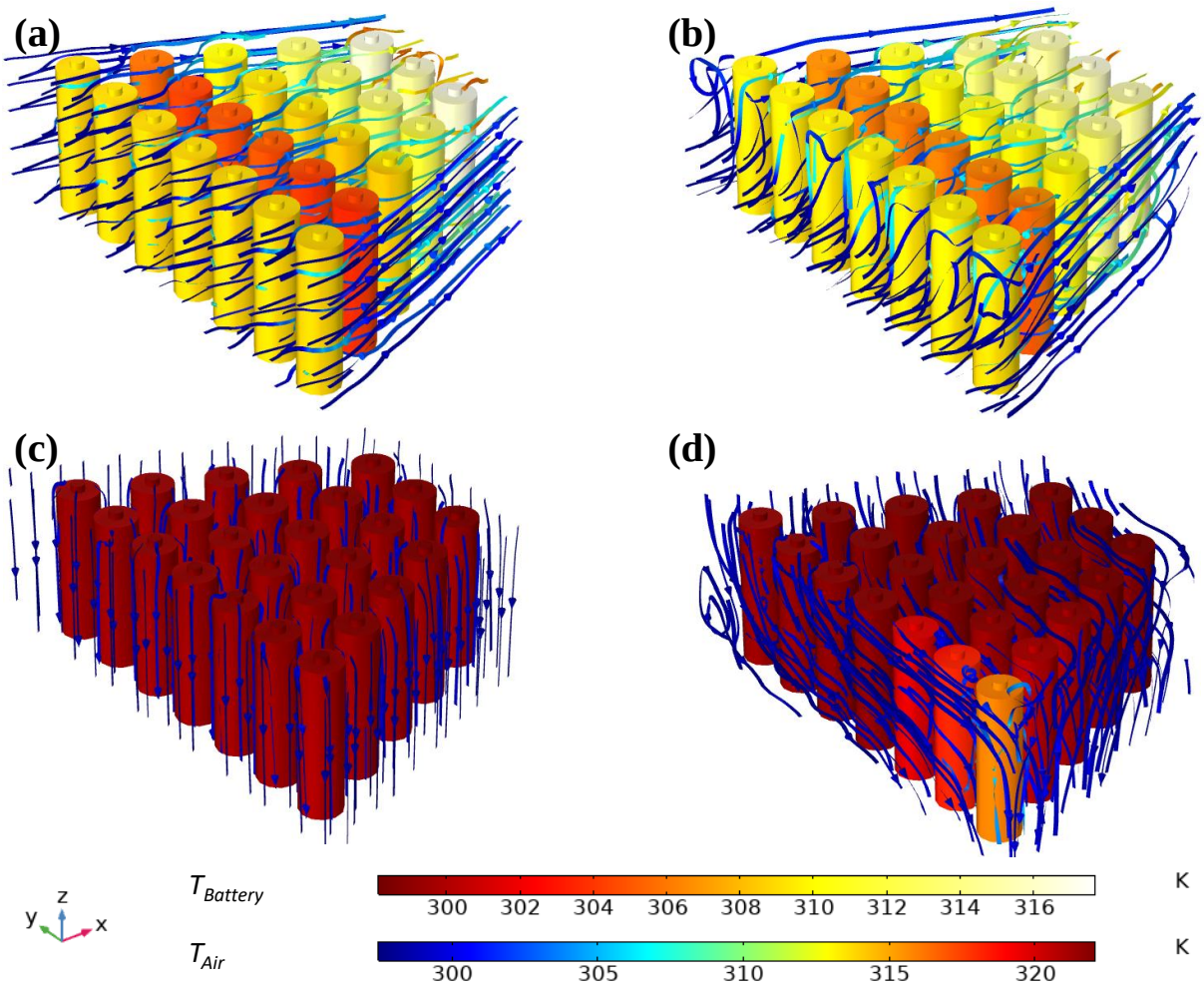

Figure S4. Temperature distribution of the battery packs with different inlet and outlet positions for trapezoid arrangement. (a) The air inlet is on the left and the outlet is on the right. (b) The air inlet is on the lower left side and the outlet is on the upper right side. (c) The air inlet is on the upper side and the outlet is on the lower side. (d) The air inlet is on the upper left and the outlet is on the lower right.

1. Yudha, C. S.; Muzayanha, S. U.; Widiyandari, H.; Iskandar, F.; Sutopo, W.; Purwanto, A., Synthesis of LiNi0.85Co0.14Al0.01O2 Cathode Material and its Performance in an NCA/Graphite Full-Battery. *Energies* **2019,** *12* (10), 1886.